Polyoxotungstate Archetype $\{P_4W_{27}\}$ and its 3d Derivatives

Tuba Iftikhar,[a, b] Natalya V. Izarova,*[a, b] Jan van Leusen,[a] and Paul Kögerler*[a, b]

Abstract: The propensity of the new, phenylphosphonate-stabilized polyoxotungstate $[(C_6H_5P^{V}O)_2P_4W_{24}O_{92}]^{16-}$ to act as a precursor for new 3d metal-functionalized polyanions has been investigated. Reactions with Mn^{II} and Cu^{II} induce the formation of the previously unknown polyoxotungstate archetype $\{P_4W_{27}\}$, isolated as salts of the polyanions $[Na\subset\{Mn^{II}(H_2O)\}\{WO(H_2O)\}P_4W_{26}O_{98}]^{13-}$ (**1**) and $[K\subset\{Cu^{II}(H_2O)\}\{W(OH)(H_2O)\}P_4W_{27}O_{99}]^{14-}$ (**2**), which were characterized in the solid state (single-crystal X-ray diffraction, elemental and TG analyses, IR spectroscopy, SQUID magnetometry) and in aqueous solution (UV/Vis spectroscopy, cyclic voltammetry).

Introduction

Polyoxotungstate (POT) structures incorporating transition metal (TM) ions and their polynuclear assemblies[1] attract significant attention as robust and efficient catalysts for various processes[2] as well as materials with interesting magnetic properties, such as pronounced magnetic anisotropy.[3]

The common synthetic strategy for new functional TM-POT assemblies includes reactions of TM salts with lacunary polyanions, i.e. incomplete derivatives of intact (and less reactive) closed-cluster shell POTs, e.g. the Wells-Dawson-type polyanion $[\alpha\text{-}P_2W_{18}O_{62}]^{6-}$.[4,5] As all-inorganic highly negatively charged species, such lacunary POTs comprise rigid and well-defined reactive sites for binding heterometals and electrophilic main groups to form products with an outstanding range of nuclearities and structural characteristics.[1–3,5–6] As discrete metal oxide particles, lacunary POT ligands typically display significant thermal and redox stability for the complexes with TMs, an important prerequisite for future applications.

Stabilization of polynuclear TM clusters with unusual structures often requires multilacunary POTs as auxiliary ligands.[6d] In recent years significant work has focused on hexalacunary derivatives of the Wells-Dawson-type phosphotungstate, $[\alpha\text{-}H_2P_2W_{12}O_{48}]^{12-}$ ($\{P_2W_{12}\}$),[7a,b] and its macrocyclic tetramer, $[P_8W_{48}O_{184}]^{40-}$ ($\{P_8W_{48}\}$).[7c] The metastable $\{P_2W_{12}\}$ polyanions offer six vacant sites able to efficiently accommodate several TM centers. The most impressive examples of $\{P_2W_{12}\}$-stabilized multinuclear TM assemblies include multi-iron complexes $[\alpha\text{-}H_4P_2W_{12}Fe^{III}{}_9O_{56}(OAc)_7]^{6-}$,[8a,b] $[H_{56}Fe^{III}{}_{28}O_{56}(P_2W_{12}O_{48})_4]^{28-}$[8a] and $[H_{55}Fe^{III}{}_{27}W^{VI}O_{56}(P_2W_{12}O_{48})_4]^{26-}$,[8a] a tetrameric niobium derivative $[\{\alpha\text{-}P_2W_{12}Nb^{V}{}_7O_{63}(H_2O)_2\}_4\{Nb^{V}{}_4O_4(OH)_6\}]^{30-}$ showing photocatalytic activity for H_2 evolution[8c] as well as $[H_{31}\{NaMn^{III}{}_{12}Mn^{II}{}_3(OH)_{12}(H_2O)_{40}\}\{\alpha\text{-}Nb^{V}{}_6P_2W_{12}O_{62}\}_6]^{10-}$ polyanions.[8d] The approximately D_{4h}-symmetric wheel-shaped $\{P_2W_{12}\}$-based tetramer, $\{P_8W_{48}\}$, has a nano-sized inner cavity able to serve as a nanoreactor or nucleation pocket for the assembly of various oxo/hydroxo clusters of transition and main group metals, such as $\{Cu^{II}{}_{20}\}$ in $[Cu^{II}{}_{20}X(OH)_{24}(H_2O)_{12}P_8W_{48}O_{184}]^{25-}$ (X = Cl, Br, I)[9a,b] and $[Cu^{II}{}_{20}(N_3)_6(OH)_{18}P_8W_{48}O_{184}]^{24-}$,[9c] $\{Fe^{III}{}_{16}\}$ in $[Fe^{III}{}_{16}(OH)_{28}(H_2O)_4P_8W_{48}O_{184}]^{20-}$,[9d] $\{Mn^{II}{}_6W^{VI}{}_4\}$ in $[(P_8W_{48}O_{184})(W_4O_{16})K_{10}Li_4Mn^{II}{}_{10}Na(H_2O)_{50}Cl_2]^{15-}$,[9e] $\{V^{V}{}_4V^{IV}{}_4\}$ in $[K_8\subset\{P_8W_{48}O_{184}\}\{V^{V}{}_4V^{IV}{}_2O_{12}(H_2O)_2\}_2]^{24-}$,[9f] and $\{Mo_4\}$ in $[K_8\subset\{P_8W_{48}O_{184}\}\{Mo^{VI}O_2\}_4\{Mo^{V}{}_4O_{10}(H_2O)_3\}_2]^{24-}$[9g] and $[K_4\subset\{Mo^{IV}{}_4O_4S_4(H_2O)_3(OH)_2\}_2(WO_2)(P_8W_{48}O_{184})]^{30-}$,[9h] as well as $\{Al^{III}{}_{16}\}$ in $[Al^{III}{}_{16}(OH)_{24}(H_2O)_8(P_8W_{48}O_{184})]^{16-}$ and $\{Ga^{III}{}_{16}\}$ in $[Ga^{III}{}_{16}(OH)_{32}(P_8W_{48}O_{184})]^{24-}$.[9i]

In contrast, the V-shaped dimer of $\{P_2W_{12}\}$, $[H_2P_4W_{24}O_{94}]^{22-}$ ($\{P_4W_{24}\}$), where two $\{P_2W_{12}\}$ units are connected via four O bridges (Supporting Information, Figure S1), hypothesized to exist already 35 years ago based on elemental analysis results,[7c] remains elusive, apparently due to its very limited solution stability, and only two heterometal complexes of $\{P_4W_{24}\}$, $[\{Sn^{IV}(CH_3)_2\}_4(H_2P_4W_{24}O_{92})_2]^{28-}$[10a] and $[W_2Co^{II}{}_2O_8(H_2O)_2(P_4W_{24}O_{92})]^{20-}$[10b] have appeared in the literature since. Recently we discovered that the $\{P_4W_{24}\}$ skeleton can be stabilized with phenylphosphonate and phenylarsonate groups, and the corresponding $[(C_6H_5X^{V}O)_2P_4W_{24}O_{92}]^{16-}$ (X = P, As) polyanions can be easily isolated as pure crystalline products.[11] Moreover, the $[(C_6H_5P^{V}O)_2P_4W_{24}O_{92}]^{16-}$ derivative ($\{P_4W_{24}(PhP)_2\}$) remains stable in aqueous solution for at least 1 to 2 hours and, thus, it has a great potential to serve as a new POT precursor, where reactions with heterometals can lead to complexes with unusual structures and properties.

Consequently, in exploring the reactivity of $\{P_4W_{24}(PhP)_2\}$ towards various heterometals at different synthetic conditions, we observed the formation of $[Na\subset\{Mn^{II}(H_2O)\}\{WO(H_2O)\}P_4W_{26}O_{98}]^{13-}$ (**1**) and $[K\subset\{Cu^{II}(H_2O)\}\{W(OH)(H_2O)\}P_4W_{27}O_{98}]^{13-}$ (**2**) with unique POT cluster structures. These were obtained upon

[a] T. Iftikhar, Dr. N. V. Izarova, Dr. J. van Leusen, Prof. Dr. P. Kögerler
Institute of Inorganic Chemistry
RWTH Aachen University, 52074 Aachen (Germany)
E-mail: paul.koegerler@ac.rwth-aachen.de

[b] T. Iftikhar, Dr. N. V. Izarova, Prof. Dr. P. Kögerler
Jülich-Aachen Research Alliance (JARA-FIT) and Peter Grünberg Institute 6
Forschungszentrum Jülich, 52425 Jülich (Germany)
E-mail: n.izarova@fz-juelich.de

Supporting information for this article is available on the WWW under https://doi.org/10.1002/chem.202004894

reaction of $\{P_4W_{24}(PhP)_2\}$ with Mn^{II} and Cu^{II} ions, respectively, in 0.5 M NaOAc (pH 4.8) at 70 °C for 72 hours and crystallized as the hydrated K^+/Na^+ salts $K_{10}Na_3[Na\subset\{Mn^{II}(H_2O)\}\{W^{VI}O(H_2O)\}P_4W^{VI}_{26}O_{98}]\cdot 26H_2O$ (**KN-1**) and $Na_{2.5}K_{10}H_{0.5}[K\subset\{Cu^{II}(H_2O)\}\{W^{VI}(OH)(H_2O)\}P_4W^{VI}_{27}O_{98}]\cdot 28H_2O$ (**KN-2**).

Results and Discussion

Crystal structure analysis

Single-crystal X-ray analysis of **KN-1** and **KN-2** revealed that the compounds are not isostructural, although both of them crystallize in the monoclinic space group *C*2/*c*, and the polyanions **1** and **2** differ only slightly in their structure (Figures 1, 2). Both comprise the unusual V-shaped $\{P_4W_{26}O_{98}\}^{20-}$ POT moiety accommodating an additional W^{VI} center, a transition heterometal ion (**1**: Mn^{II}, **2**: Cu^{II}) and a single alkali metal ion in its inner cavity (**1**: Na^+, **2**: K^+).

The structure $\{P_4W_{26}O_{98}\}^{20-}$ formally represents a C_{2v}-symmetric, V-shaped $\{P_4W_{24}\}$ dimer, where each non-bound $\{W_2O_{10}\}$ terminals of its $\{\alpha\text{-}P_2W_{12}\}$ subunits binds an additional octahedrally coordinated W^{VI} center (W_{term}), thus, forming $\{W_3O_{13}\}$ "caps" (see Figure S1). Alternatively, it can be considered as a dimer of two *pentalacunary* derivatives of Wells-Dawson phosphotungstates, $\{\alpha\text{-}P_2W_{13}O_{51}\}$, connected to each other via four W–O–W bridges (W–O: 1.842(13)–1.975(14) Å in **1**, 1.874(13)–1.955(14) Å in **2**; see Figure S2).

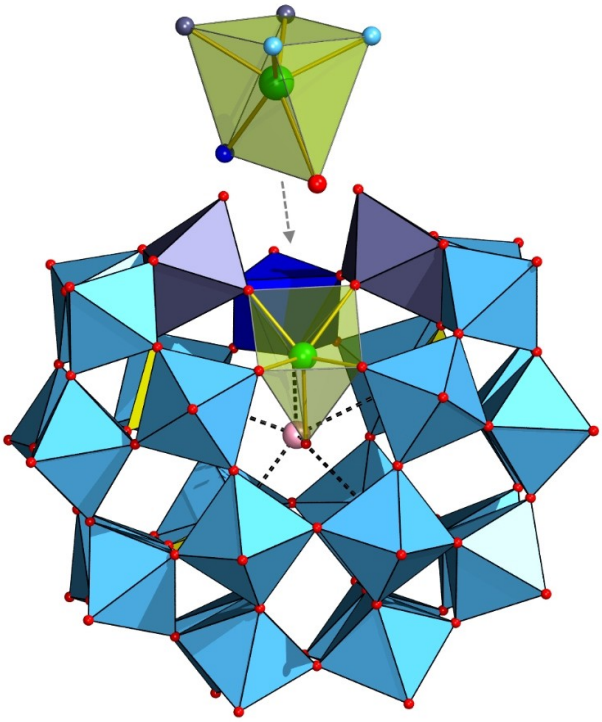

Figure 1. Structure of polyanion **1**, emphasizing the structural relation to the V-shaped $\{P_2W_{12}\}_2$ dimer substructure, shown as light-blue WO_6 and yellow PO_4 polyhedra. The $W_{term}O_6$ octahedra, sharing edges with the upper $\{P_2W_{12}\}$ ends, are emphasized in gray-blue. The additional $W_{cav}O_6$ octahedron (dark blue) bridges both the $\{P_2W_{12}\}$ groups and the two $\{W_{term}\}$ units in corner-sharing mode. A $Mn^{II}(OH_2)$ group is present in the front half of the cavity and forms a trigonal-prismatic MnO_6 environment (upper inset, the O sites here are colored according to the WO_6 octahedra they belong to, the remaining red O position represents the water ligand). A Na^+ cation (rose sphere) is present in the central cavity. Mn: green, O: red.

The W^{VI} ion (W_{cav}) located in the cavity of $\{P_4W_{26}O_{98}\}^{20-}$ exhibits a distorted octahedral coordination geometry. In both structures it binds two oxygen atoms of the $\{W_3O_{13}\}$ "caps" (one atom from each "cap") in *cis* geometry (W_{cav}-O: 1.83(3) Å in **1**, 1.865(14)–1.900(14) Å in **2**) as well as two oxygen atoms of the $\{PW_4\}$ "belts" (W_{cav}-O: 2.087(14)–2.091(14) Å in **1**, 1.988(13)–1.994(12) Å in **2**), one from each $\{\alpha\text{-}P_2W_{13}O_{51}\}$ subunit (Figures 1, 2). In **1** its coordination environment is completed by a μ_2-O atom bridging it to a Mn^{II} ion (W_{cav}-O: 1.85(3) Å, Mn–O: 2.24(3) Å) and a *trans*-positioned terminal aqua ligand (W_{cav}-O_{aq}: 2.23(3) Å). In **2** the central W_{cav} coordinates a terminal aqua ligand (W_{cav}-O_{aq}: 2.18(3), 2.23(3) Å) directed into the cluster cavity, as well as an outward-pointing terminal hydroxo ligand (W_{cav}-O(H): 1.927(18), 2.013(19) Å), see Tables S2 and S3 for bond valence sums,[12] in addition to four O sites of the $\{P_4W_{26}O_{98}\}^{20-}$ moiety.

The Mn^{II} center in **1** adopts the vacant coordination site of $\{P_4W_{27}\}$ neighboring the W_{cav} site. Its O_6 coordination environment here is trigonal prismatic: one triangular face is composed of two O atoms of the $\{W_3O_{13}\}$ "caps" (Mn–O: 2.24(2)–2.31(3) Å) and the μ_2-O atom bridging it to W_{cav}, while the other O_3 triangle is defined by two oxygens of the $\{PW_4\}$ "belts" (Mn–O: 2.165(15)–2.223(16) Å) and a terminal water ligand (Mn-O_{aq}: 2.373(14) Å). The Mn···W_{cav} distance here amounts to 3.826 Å. Note that the binding mode of the central W^{VI} ion in **1** and **2** is highly reminiscent of that observed in the inner $\{W_5O_5\}$ ring of the seminal polyanion $[Na\subset P_5W_{30}O_{110}]^{14-}$. Like in this POT, the $\{W_5O_5\}$ ring in **1** is occupied by a Na^+ cation which additionally weakly binds to the aqua ligand of Mn^{II} (Figures 1 and S3).

The Cu^{II} ion in **2** is five-coordinated and exhibits a distorted tetragonal pyramidal coordination geometry. It binds four O atoms of the $\{P_4W_{26}O_{98}\}^{20-}$ polyanion (Cu–O: 1.864(14)–1.994(12) Å) as well as an outwards-looking terminal aqua ligand (Cu-O_{aq}: 1.927(13), 2.013(19) Å). At 4.920 Å, the W_{cav}···TM (Cu/Mn) distance in **2** is significantly longer than in **1**. The central K^+ ion in **2** is located closer to the side of the $\{CuW_4O_5\}$ ring and interacts with a terminal aqua ligand on W_{cav}, as well as with μ_3-$O_{(P,2W)}$ atoms of both $\{\alpha\text{-}P_2W_{13}O_{51}\}$ building blocks of the $\{P_4W_{26}O_{98}\}$ skeleton (Figures 2 and S4).

Given the condensed structure of the POT fragment in **1** and **2** these structures should be considered as transition metal complexes of a previously unknown POT archetype $\{H_xP_4W_{27}O_{100}\}^{(18-x)-}$, which are obtained relatively easily and reproducibly from the $\{P_4W_{24}(PhP)_2\}$ precursor. Formation of such species would require dissociation of the phenylphosphonate groups from the POT precursor, which is not surprising considering that the reaction mixture was heated to 70 °C for 3 days, as well as completion of the POT skeleton by additional W^{VI} ions that form in the course of the decomposition of a part of the precursor. While the exact mechanism for formation of **1** and **2** from $\{P_4W_{24}(PhP)_2\}$ remains unknown, we conjecture that the short-term solution stability of this POT precursor (several

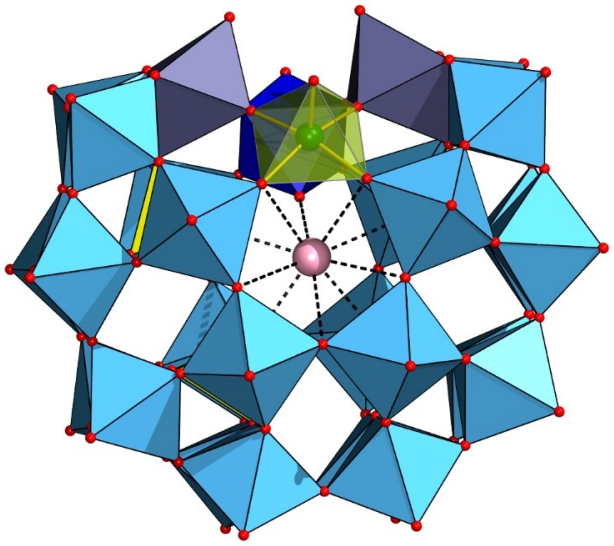

Figure 2. Structure of polyanion **2** with color code as in Figure 1. In contrast to **1**, a Cu^{II} ion with an exo-oriented water ligand here is attached to the O_4 environment of the upper cavity, the central cavity hosts a K^+ cation (rose sphere).

hours at room temperature) allows for rapid coordination of the transition metal ions in the central cavity of at least part of the polyanions leading to stabilization of the dimeric POT assembly. Concurrent dissociation of the organophosphonate groups accompanied by a decomposition of non-coordinated POT species allows the condensation of additional W^{VI} centers to TM-stabilized POT units resulting in {TM-P_4W_{27}} products. Interestingly, similar reactions of {$P_4W_{24}(PhP)_2$} with Co^{II} at the same reaction conditions resulted in chain-like $\{[Co(H_2O)_4]_2[\{(H_2O)_4Co\}(C_6H_5PO)_2P_4W_{24}O_{92}]\}_n^{10n-}$ assemblies[13] that we previously reported.[11] This finding supports the hypothesis on rapid binding of TM ions in the central cavity of {$P_4W_{24}(PhP)_2$} precursor. In case of Co^{II} this binding is probably more efficient and, thus, allows stabilization of most (or almost all) of the {$P_4W_{24}(PhP)_2$} POT skeletons. This would exclude the presence of free tungstate ions in reaction solution in the amounts sufficient to formation of {$Co^{II}P_4W_{27}$} complexes, and, hence, would allow rebuilding the organophosphonate-decorated species upon cooling of the reaction mixture. This difference in apparent behaviour of these transition metal ions is likely linked to the difference in their ionic radii. We hypothesize that the size of Co^{II} may fit particularly well for the stabilization of the adduct with {$P_2W_{24}(PhP)_2$}, while for Mn^{II} and Cu^{II} the {MP_4W_{27}} complexes appear to be more stable than the corresponding {$P_2W_{24}(PhP)_2$} derivatives.

These compounds cannot be synthesized by the direct use of the amorphous compound that had been tentatively attributed to contain $[H_2P_4W_{24}O_{94}]^{22-}$ in the 1985 paper,[7c] or [α-$H_2P_2W_{12}O_{48}$]$^{12-}$ under otherwise identical synthetic conditions. Instead, crystals of Wells-Dawson POT, [α-$P_2W_{18}O_{62}$]$^{6-}$, have been isolated. The groups of Li and Wang in 2008 reported formation of $[W_2Co^{II}{}_2O_8(H_2O)_2(P_4W_{24}O_{92})]^{20-}$ POTs with overall related structures, which were obtained by reaction of Co^{II} ions and hexalacunary [α-$H_2P_2W_{12}O_{48}$]$^{12-}$ polyanions in aqueous acetic acid solution (H_2O:CH_3COOH = 2:1) at pH 3.[10b] However in these species there is an uncontrolled disorder between Co^{II} and W^{VI} ions: the site occupancy factors (s.o.f.) of the additional atoms in the {MW_2O_{13}} "caps" are 0.25 for Co^{II} and 0.75 for W^{VI}, while the s.o.f. of the atoms in the central positions are 0.75 for Co^{II} and 0.25 for W^{VI}. At the same time, in our case the composition of the polyanions **1** and **2** and the exact location of the transition metal ion is clearly defined, and the observed disorder between TM ion and W^{VI} ion in the central position with equal s.o.f. of 0.5 in every case is caused solely by two possible orientations of the polyanions in the crystal lattice.

IR spectroscopy

ATR FT-IR spectra of **KN-1** and **KN-2** performed on solid materials exhibit a good match to each other reflecting a similarity of POT skeletons in these compounds. In comparison to the ATR spectrum of **KLD-{$P_4W_{24}(PhP)_2$}** precursor (Figure S5), three distinct bands at around 1085, 1018 and 989 cm^{-1} corresponding to P–O vibrations are present in the spectra of all three samples, while another P–O bonds-associated band appearing at 1151 cm^{-1} in the spectrum of the precursor is much more intense and is shifted to 1161 cm^{-1} in the spectra of **KN-1** and **KN-2**. The bands at 1128 and 971 cm^{-1} attributed to P–C and P–O vibrations of phenylphosphonate groups in **KLD-{$P_4W_{24}(PhP)_2$}** are not seen in the spectra of **KN-1** and **KN-2** although their spectra exhibit a weak band at around 1135 cm^{-1} that might belong to P–O fingerprints of the {P_4W_{27}} archetype. A sharp band at around 900–910 cm^{-1} corresponds to terminal W=O vibrations, while other peaks in the region from 900 to 450 cm^{-1} are characteristic for W–O-W, W–O-P and W–O-M vibrations.

The signals at 1614 cm^{-1} (**KN-1** and **KN-2**) and 1620 cm^{-1} (**KLD-{$P_4W_{24}(PhP)_2$}**) belong to asymmetrical vibrations of co-crystallized water molecules in these compounds. The bands in the area from 1600 to 1200 cm^{-1} in the spectrum of the precursor belong to vibrations of C–N bonds of dimethylammonium countercations and therefore are logically absent in the spectra of **KN-1** and **KN-2**.

Thermogravimetric analysis

Thermogravimetric analysis on **KN-1** and **KN-2** (25 to 450 °C under N_2 flux) showed a major weight loss step from room temperature up to around 250 °C for **KN-1** (-5.3% total mass) and 350 °C for **KN-2** (-6.1%). For **KN-1** this weight loss is gradually continued up to 450 °C (the total weight loss from RT go 450 °C is −6.3%) and up to 500 °C for **KN-2** (-6.5% from RT; see Figures S6, S7). These correspond to the loss of weakly bound crystal water molecules (calculated: −6.0% and −6.1% for **KN-1** and **KN-2**, respectively) as well as to the much stronger bound aqua and hydroxo ligands on the central TM and W^{VI} ions in **1** and **2** (calculated: −0.5% for **KN-1** and −0.6% for **KN-2**), respectively.

Table 1. Electrode potential values of the redox couples observed in CVs for **KN-1** and **KN-2** in 0.5 M NaOAc buffer (pH 4.8) vs. Ag/AgCl and RHE.

Process	*Heterometal-associated redox processes*						*$W^{VI/V}$-associated processes*				
Sample	E_{ox}, V ($Mn^{II/IV}$)	E_{red}, V ($Mn^{IV/III}$)	E_{red}, V ($Mn^{III/II}$)	$E_{1/2}$, V ($Cu^{II/I}$)	E_{red}, V ($Cu^{I/0}$)	E_{ox}, V ($Cu^{0/II}$)	$E_{1/2}^{I}$, V	$E_{1/2}^{II}$, V	$E_{1/2}^{III}$, V	$E_{1/2}^{IV}$, V	$E_{1/2}^{V}$, V
vs. Ag/AgCl											
KN-1	+0.82	+0.78	+0.71	–	–	–	−0.405	−0.535	–	−0.735	−0.850
KN-2				−0.030	−0.18	+0.06	−0.305	−0.485	−0.57	−0.745	−0.845
vs. RHE											
KN-1	+1.30	+1.26	+1.19	–	–	–	+0.075	−0.055	–	−0.255	−0.370
KN-2	–	–	–	+0.450	+0.300	+0.486	+0.175	−0.005	−0.090	−0.265	−0.365

Solution studies

UV/Vis spectroscopy

UV/Vis absorption spectra (see Figures S8 and S9) were recorded for **KN-1** and **KN-2** solutions in 0.5 M NaOAc buffer (pH 4.8). They show similar absorption maxima in the UV region at around 225 nm ($\varepsilon = 1.3\times10^{6}\ M^{-1}cm^{-1}$ for both **1** and **2**) and at 275 nm ($\varepsilon = 6.8\times10^{5}\ M^{-1}cm^{-1}$ for **1** and **2**), which reflect characteristic ligand-to-metal charge transitions (LMCT) from the pπ ($O_{terminal}$) to dπ* (W) in the W=O bonds as well as dπ-pπ-dπ electronic transitions in the W–O-W bonds of the POT units.

In addition, the spectrum of **KN-1** shows two absorption maxima in the visible region at 353 nm ($\varepsilon = 6.4\times10^{4}\ M^{-1}cm^{-1}$) and 394 nm ($\varepsilon = 4.2\times10^{4}\ M^{-1}cm^{-1}$), which correspond to CT and weak spin-forbidden d-d transitions of the Mn^{II} centers (see Figure S8, inset). The spectrum of **KN-2** also exhibits a low intensity absorption maximum in the visible light area at around 770 nm ($\varepsilon = 1.3\times10^{2}\ M^{-1}cm^{-1}$), attributed to the d-d transitions of the Cu^{II} ions in **2** (see inset on Figure S9).

Time-series measurements on **KN-1** solution in 0.5 M NaOAc buffer (pH ~4.8) suggest that polyanions **1** are fairly stable in this medium for at least one day (see Figures S10, S11). The spectra of **KN-2** in the same medium did not show any change in the UV region (Figure S12), while the intensity of the absorption maximum in the visible light area gradually increases with time (Figure S13). The change of the spectrum becomes especially pronounced after 3 hours. This suggests that the Cu^{II} ions are slowly released from polyanions **2** in the 0.5 M NaOAc (pH 4.8) medium, possibly without immediate decomposition of the POT skeleton. Nevertheless, the stability of polyanions **2** in 0.5 M NaOAc buffer was sufficient to conduct electrochemistry measurements on these species.

Cyclic voltammetry

Cyclic voltammograms for **KN-1** and **KN-2** were recorded at room temperature in 0.5 M NaOAc medium (pH 4.8) on 0.5 mM solutions. The obtained curves for the both compounds exhibit redox couples, which (1) correspond to the reduction and reoxidation processes in the POT skeleton, as well as (2) are associated with the redox activity of the corresponding TM ion.

For **1** the processes of the two types are well separated from each other. Thus, the cyclic voltammogram for the Mn^{II} derivative exhibits four reversible redox couples associated with reduction of W^{VI} centers in **1** to W^{V} and their reoxidation (see Table 1 for the redox potentials) in the negative potential domain. In addition, it shows an anodic wave at around +0.82 V *vs.* Ag/AgCl (20 mV/s), which could be attributed to the $Mn^{II/IV}$ oxidation process based on comparison with the electrochemical data for other Mn-containing POTs.[14] Its reduction counterpart is observed at around +0.71 V *vs.* Ag/AgCl. At slow scan rates (10 mV/s) one can notice that this relatively broad wave is getting split in two waves located at +0.78 V and +0.71 V *vs.* Ag/AgCl, which presumable correspond to $Mn^{IV/III}$ and the following $Mn^{III/II}$ reduction processes (see Figures 3 and S14), respectively. The peak currents for all the reduction and oxidation processes as a function of the square root of the potential scan rate show perfect linearity (see Figures S15–S18 and Tables S4, S5), indicating diffusion-controlled electrode reactions.

The redox couples in the cyclic voltammogram of **KN-2** are mainly located in the negative potential domain (Figure 4). The first redox process centered at −0.0295 V *vs.* Ag/AgCl (ΔE = 0.045 V at 20 mV/s) could be attributed to the (quasi)reversible Cu^{II} to Cu^{I} reduction. It is followed by a reduction of the formed

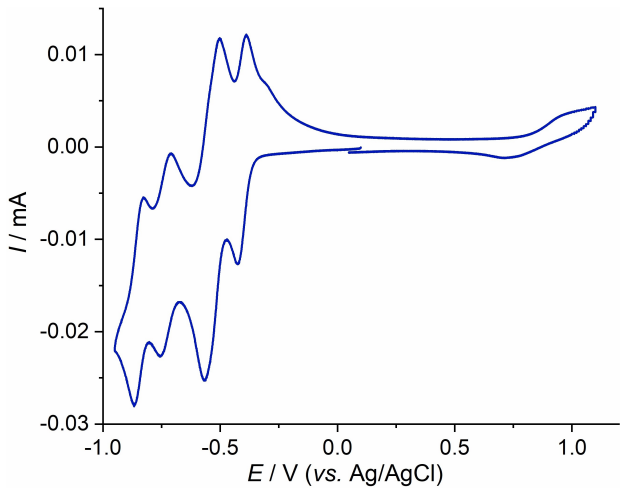

Figure 3. Room-temperature cyclic voltammogram of a 0.5 mM solution of **KN-1** in 0.5 M NaOAc (pH 4.8) at 20 mV/s.

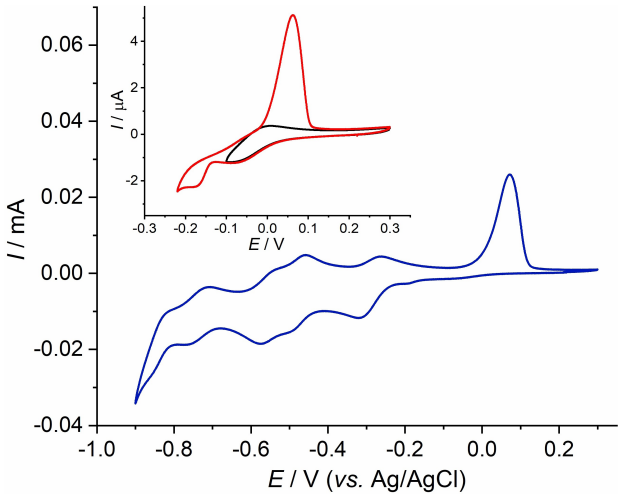

Figure 4. Room-temperature cyclic voltammogram of a 0.5 mM solution of **KN-2** in 0.5 M NaOAc (pH 4.8) at 20 mV/s. Inset: the cyclic voltammograms restricted to −0.22 V and −0.1 V (at 20 mV/s).

Cu^{I} ions into Cu^{0} at −0.18 V *vs.* Ag/AgCl which is paired with a sharp anodic wave at +0.06 V *vs.* Ag/AgCl corresponding to reoxidation of the metallic Cu^{0} to Cu^{II} ions. The shape of this wave and a much higher current corresponding to $Cu^{0/II}$ reoxidation in comparison with all other anodic waves suggests a surface-confined process. The release of the Cu^{II} ions from the polyanion and precipitation of the metallic cupper on the working electrode also could be well seen from the comparison of the first and second redox cycles showing a slight shift and increase of the intensity of the Cu^{II} to Cu^{I} reduction process (see Figure S19). Such electrochemical behavior is not unusual for Cu^{II}-containing POTs and is well comparable with the data reported for other Cu^{II}-POT derivatives.[9b,c; 15] We note that the CV curves restricted to −0.1 V recorded directly after polishing of the electrode and after scanning in the potential area below −0.18 V *vs.* Ag/AgCl (after complete Cu^{II}/Cu^{0} reduction) for 20–30 min are very similar (Figure S20). Moreover, the latter CV curve does not show any anodic processes at around +0.06 V *vs.* Ag/AgCl. This indicates that reoxidation and re-dissolution of the metallic copper (deposited on the electrode as a result of the reduction process) seems to be complete upon the reverse scan.

The Cu-associated redox waves in the cyclic voltammogram of **2** are accompanied by five redox couples associated with reversible and quasi-reversible $W^{VI/V}$ reductions (see Table 1 for $E_{1/2}$). The linear dependence of the reduction and oxidation currents for the $W^{VI/V}$ and $Cu^{II/I}$ processes with respect to the square root of the scan rate is evident of their diffusion-controlled character (see Figures S21–S24 and Table S6). The positions and intensity of the W-associated part of the cyclic voltammogram remain unchanged over six cycles (Figure S25) indicating a stability of the POT skeleton in line with the time-dependent UV spectra for these polyanions in the same medium.

The small separations between the reduction and oxidation potentials attributed to the electrochemical activity of W^{VI} centers in **1** and **2** suggest involvement of multiple electrons in these processes which is possible when several W^{VI} of the same (or similar) structural types are reduced simultaneously. Such behavior is not unexpected as is commonly observed for large POT systems.[16]

A comparison of the CV curves of **1** and **2** (see Figure S26) shows that the position of the two redox waves in the potential range between −1.0 and −0.7 V *vs.* Ag/AgCl is nearly identical. At the same time, the redox couple appearing at −0.535 V *vs.* Ag/AgCl in the cyclic voltammogram of the Mn^{II} derivative, is split in two processes centered at −0.57 V and −0.485 V *vs.* Ag/AgCl in the CV curve of **2**, while the wave at −0.405 V seen in the CV curve for **1** is significantly shifted to the more positive potential (−0.305 V *vs.* Ag/AgCl) for the Cu^{II} derivative. This allows to propose that this latter wave corresponds to the W^{VI} centers that are directly linked to the TM ions via O bridges. In case of **2** the release of the reduced Cu^{II} ions from the POT skeleton would logically result in the decrease of its overall stability, that most likely could be the reason for the lowering of the first reduction potential of W^{VI} centers in polyanions **2**. Consequently, the waves at $E < -0.7$ V *vs.* Ag/AgCl should be attributed to the W^{VI} which are distant from the heterometal ion and are less affected by the structural modifications related to the different coordination geometries of the metal ions incorporated in the inner cavity of $\{P_4W_{26}O_{98}\}^{20-}$.

Magnetochemistry

The field- and temperature dependence of the magnetic susceptibility of **KN-1** and **KN-2** were measured using SQUID magnetometry and are shown in Figure 5. For **KN-1**, $\chi_m T$ is 4.40 cm^3 K mol^{-1} at 290 K and 0.1 T (Figure 5a), i.e. within the expected range of 3.99-4.65 cm^3 K mol^{-1} of a single high-spin $3d^5$ Mn^{2+} center.[17a] Upon decreasing the temperature, $\chi_m T$ remains almost constant down to about 15 K. At lower temperatures, $\chi_m T$ drops off reaching 4.06 cm^3 K mol^{-1} at 2.0 K. At this temperature, the molar magnetization rapidly increases for fields below 2 T, and indicates saturation effects for higher fields. At 5.0 T, the M_m value of 4.9 $N_A\,\mu_B$ is slightly below the expected saturation value of 5.0 $N_A\,\mu_B$ deduced from $\chi_m T$ data at 290 K ($M_{m,sat} = g_{eff} S\, N_A\,\mu_B$, $S = 5/2$, $g_{eff} \approx 2.0$). Considering the isotropic spin-like behavior of $3d^5$ centers even in slightly distorted trigonal prismatic ligand field environments, the data indicate very small antiferromagnetic exchange interactions due to the drop off observable at rather high $T \approx 15$ K, since a relevant zero-field splitting can be excluded. In addition, the Zeeman effect at a magnetic field of 0.1 T is too small to cause such a behavior.

For **KN-2**, the room temperature value of $\chi_m T$ at 290 K of 0.516 $cm^3\,K\,mol^{-1}$ (Figure 5b) lies within the range of 0.361−0.605 $cm^3\,K\,mol^{-1}$ expected for a single $3d^9$ Cu^{2+} center.[17a] Upon cooling, $\chi_m T$ continuously decreases down to about 15 K (as **KN-1**), and subsequently drops off to 0.432 $cm^3\,K\,mol^{-1}$ at 2.0 K. M_m increases to 1.1 $N_A\,\mu_B$ at 5.0 T at

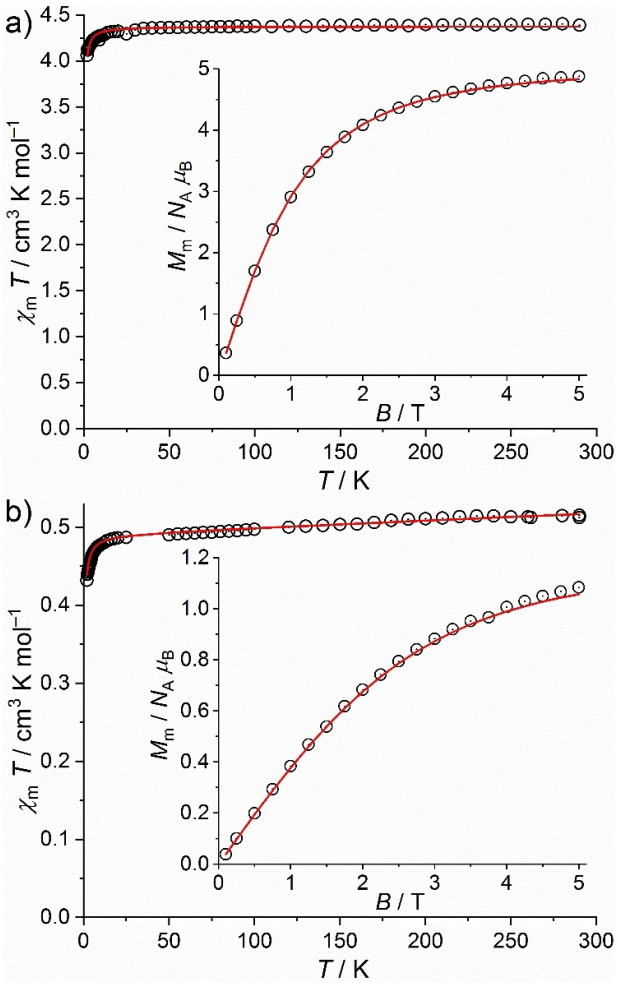

Figure 5. SQUID measurements and fitting: (a) $\chi_m T$ vs. temperature T at 0.1 T; inset: molar magnetization M_m vs. applied field B at 2.0 K of **KN-1**; (b) same of **KN-2**; experimental data (symbols) and least squares fit (solid lines).

this temperature showing the onset of saturation, which is estimated to be about 1.2 N_A μ_B ($S=1/2$, $g_{eff} \approx 2.3$). A slight deviation from spin-like behavior, i.e. a small slope of $\chi_m T$ vs. T and a minor drop off at low temperatures, is expected for a $3d^9$ center with a Jahn-Teller-distorted octahedral (or a square-pyramidal) ligand field due to interelectronic repulsion and spin-orbit coupling. However, the presence of very small intermolecular antiferromagnetic exchange interactions as for **KN-1** cannot be excluded, given closest inter-cluster Mn···Mn distances of ca. 7 Å in the crystal lattice.

To gain further insight into the magnetic properties, we modeled the data employing the computational framework CONDON.[18] In order to avoid over-parametrization, for **KN-1** we assumed D_{3h} symmetry as approximation of the local ligand field symmetry, and considered all 252 microstates of a d^5 electron configuration as well as the values for the Racah parameters B and C and the one-electron spin-orbit coupling constant ζ_{3d} given in Table 2. For potential intermolecular exchange interactions, we applied the mean field model for z next-neighbor centers using the "-2J notation" of the Heisenberg Hamiltonian. The least-squares fit ($SQ=0.6\%$, relative root mean square error) yields the solid lines in Figure 5a and the parameters given in Table 2. The determined mean field parameter reveals marginal intermolecular antiferromagnetic exchange interactions within the error margin.

Table 2. Parameters of the magnetic data fits of **KN-1** and **KN-2** with Racah parameters B and C and one-electron spin-orbit coupling constants ζ_{3d},[17b] ligand field parameters B^k_q in Wybourne notation.

Sample	KN-1	KN-2
B/cm^{-1}	930	1238
C/cm^{-1}	3325	4659
ζ_{3d}/cm^{-1}	347	829
B^2_0/cm^{-1}	-4747 ± 72	619 ± 16
B^4_0/cm^{-1}	19033 ± 73	22609 ± 68
B^4_4/cm^{-1}	–	14408 ± 17
$-2zJ$/cm^{-1}	0.03 ± 0.02	0.39 ± 0.02
SQ	0.6 %	1.1 %

For **KN-2**, we assumed C_{4v} symmetry as approximation of the local ligand field symmetry considering all 10 microstates of a d^9 electron configuration and the Racah parameters and one-electron spin-orbit coupling constant shown in Table 2 We also applied the mean field model. A least-squares fit ($SQ=1.1\%$) yields the solid lines in Figure 5b and the corresponding parameters listed in Table 2. Intermolecular exchange interactions are very small and antiferromagnetic, as anticipated. Note that due to the Heisenberg Hamiltonian $H_{ex} \propto S_1 \times S_2$, a factor of about 25 should be considered in a comparison of the J values, since the spins are $S=5/2$ (**KN-1**) and 1/2 (**KN-2**).

Conclusion

The organophosphonate-stabilized polyoxoanion $[(C_6H_5P^VO)_2P_4W_{24}O_{92}]^{16-}$ can serve as a convenient precursor to the transition metal-containing polyanions of a new structural type based on the unique $\{H_xP_4W_{27}O_{100}\}^{(18-x)-}$ POT archetype. Polyanions $[Na\subset\{Mn^{II}(H_2O)\}\{WO(H_2O)\}P_4W_{26}O_{98}]^{13-}$ (**1**) and $[K\subset\{Cu^{II}(H_2O)\}\{W(OH)(H_2O)\}P_4W_{27}O_{98}]^{13-}$ (**2**) have been isolated and thoroughly characterized in the solid state and in aqueous solution. The V-shaped $\{P_4W_{27}\}$ substructure represents an extended, and apparently sufficiently more stable, version of the elusive $\{P_2W_{12}\}_2$ dimer. Their electrochemical behavior is characterized by multiple (quasi)reversible redox transformations associated with POT skeleton as well as the heterometal ions. The magnetic properties are in line with a single Mn^{2+}/Cu^{2+} center per polyanion. As these discoveries underline that organophosphonate-functionalized polyoxotungstates can indeed lead to unusual cluster structures, we currently are exploring the reactivity of $\{P_4W_{24}(PhP)_2\}$ towards other transition and rare-earth metal ions.

Experimental Section

Starting materials: The POT precursor $K_{3.5}Li_8[(CH_3)_2NH_2]_{4.5}[(C_6H_5PO)_2P_4W_{24}O_{92}]\cdot 35H_2O$ (**KLD-{$P_4W_{24}(PhP)_2$}**)

was synthesized as previously reported[11] and its identity and purity were confirmed by IR spectroscopy. All other reagents were obtained from commercial sources and were used without further purification. 0.5 M NaOAc buffer medium (pH = 4.8) was prepared by basification of 0.5 M aqueous solution of CH_3COOH (initial pH = 1.8) with solid NaOH until pH 4.8.

Analytic methods: Elemental analyses (ICP-OES, IC and C, H, and N) were performed by the Central Institute for Engineering, Electronics, and Analytics (ZEA-3), Forschungszentrum Jülich GmbH (Jülich, Germany). Thermogravimetric analyses (TGA) were carried out with a Mettler Toledo SDTA 851 (**KN-2**) and on a NETZSCH TG 209F1 Libra (**KN-1**) instruments in a dry N_2 flux (60/20 mL min^{-1}) at a heating rate of 5 K min^{-1}. ATR spectra were recorded on Bruker Vertex 70 and Avatar 360 spectrometers on solid samples. UV/Vis spectra were measured using 10 mm quartz cuvettes on a Shimadzu UV-3600plus UV-Vis-NIR spectrophotometer.

Room temperature cyclic voltammograms were recorded on ~0.5 mM solutions of **KN-1** and **KN-2** in 0.5 M NaOAc buffer (pH = 4.8), prepared by addition of solid NaOH sample in 0.5 M aqueous CH_3COOH solution until pH 4.8, using an SP-150 potentiostat (Bio-Logic Science Instruments) controlled by EC-Lab software. The conventional three-electrode electrochemical cell included a glassy carbon working electrode with the diameter of 3 mm, a platinum wire counter electrode and an aqueous Ag/AgCl (3 M NaCl) reference electrode (0.196 V *vs.* SHE determined by measuring $[Fe(CN)_6]^{3/4-}$ as an internal standard). The solutions were thoroughly de-aerated with pure argon and kept under a positive Ar pressure during the experiments. Alumina powder was used for the cleaning of the working electrode which was then thoroughly rinsed with deionized water. Redox potentials were defined from the average values of the anodic and cathodic peak potentials and reported *vs.* the Ag/AgCl reference electrode.

Magnetic data were recorded using a Quantum Design MPMS-5XL SQUID magnetometer. The polycrystalline samples were compacted and immobilized into cylindrical PTFE capsules. The data were acquired as a function of the magnetic field (0.1–5.0 T at 2.0 K) and temperature (2.0–290 K at 0.1 T). They were corrected for the diamagnetic contributions of the sample holders and the compounds including a TIP contribution of the POT scaffold ($\chi_{m,TIP} = +2.62\times10^{-3}$ $cm^3 mol^{-1}$, **KN-1**: $\chi_{m,dia}/10^{-3}$ $cm^3 mol^{-1} = -1.04$, **KN-2**: -1.05).

Synthesis of $K_{10}Na_3[Na\subset\{Mn^{II}(H_2O)\}\{WO(H_2O)\}P_4W_{26}O_{98}]\cdot 26H_2O$ (KN-1): A solution of $MnCl_2\cdot 4H_2O$ (0.055 g, 0.28 mmol) in 0.5 M NaOAc (pH 4.8; 5 mL) was added to a solution of **KLD-{$P_4W_{24}(PhP)_2$}** (0.1 g, 0.014 mmol) in 0.5 M NaOAc (pH 4.8; 10 mL) under a vigorous stirring at 70 °C. The resulting reaction mixture with pH 4.6 was then placed in an oven and kept at 70 °C for 3 days. After that, the obtained reaction solution was cooled down to room temperature, following by addition of 1 M aqueous KCl solution (2 mL). The resultant yellow solution was divided into four equal portions and left for evaporation in open vials. Light-yellow block-shaped crystals of the product appeared after 2 weeks. The crystals were collected by filtration and dried in air. Yield: 0.035 g (32% based on **KLD-{$P_4W_{24}(PhP)_2$}**).

Elemental Analysis: Calculated for $H_{56}K_{10}MnNa_4O_{127}P_4W_{27}$ (found): H, 0.73 (0.73); K, 5.07 (5.02); Mn, 0.71 (0.74); Na, 1.19 (1.12); P, 1.61 (1.58); W, 64.3 (62.1) %*. IR spectrum (ATR, crystalline material), cm^{-1}: 3436 (br); 1614 (m); 1162 (m); 1086 (m); 1020 (m); 989 (m); 954 (m); 912 (m); 892(s); 765 (s); 665 (s, br); 570 (s); 520 (s); 468 (s). UV/Vis spectrum (0.5 M NaOAc; pH 4.8): $\lambda = 225$ nm, $\varepsilon = 1.3\times10^6$ $M^{-1}cm^{-1}$; $\lambda = 273$ nm, $\varepsilon = 6.8\times10^5$ $M^{-1}cm^{-1}$, $\lambda = 353$ nm, $\varepsilon = 6.4\times10^4$ $M^{-1}cm^{-1}$; $\lambda = 394$ nm, $\varepsilon = 4.2\times10^4$ $M^{-1}cm^{-1}$.

Synthesis of $Na_{2.5}K_{10}H_{0.5}[K\subset\{Cu^{II}(H_2O)\}\{W(OH)(H_2O)\}$-$P_4W_{26}O_{98}]\cdot 28H_2O$ (KN-2):

The synthetic procedure for preparation of **KN-2** is similar to that for **KN-1** except for the use of $CuCl_2\cdot 2H_2O$ (0.048 g, 0.28 mmol) instead of $MnCl_2\cdot 4H_2O$. Light-green crystals of **KN-2** possessing a block-like shape were collected by filtration and air-dried. Yield: 0.038 g (35% based on **KLD-{$P_4W_{24}(PhP)_2$}**).

Elemental Analysis: Calculated for $H_{61.5}CuK_{11}Na_{2.5}O_{129}P_4W_{27}$ (found): H, 0.80 (0.87); Cu, 0.82 (0.93); K, 5.54 (5.61); Na, 0.74 (0.67); P, 1.60 (1.64); W 63.93 (61.4) %*. IR spectrum (ATR, crystalline material), cm^{-1}: 3444 (br); 1614 (m); 1161 (m); 1136 (w); 1083 (m); 1014 (m); 987 (m); 900 (m); 783 (s); 670 (s, br); 569 (s); 520 (s); 463 (s). UV/Vis spectrum (0.5 M NaOAc; pH 4.8): $\lambda = 224$ nm, $\varepsilon = 1.31\times10^6$ $M^{-1}cm^{-1}$; $\lambda = 269$ nm, $\varepsilon = 6.74\times10^5$ $M^{-1}cm^{-1}$, $\lambda = 770$ nm, $\varepsilon = 1.28\times10^2$ $M^{-1}cm^{-1}$.

* We note that deviations of found mass percentage for W arise from intrinsic analysis limitations (specifically, during preparation of the analytical solution a part of W^{VI} ions tends to precipitate as colloidal W oxides particles leading to lower-than-actual W percentage). Nevertheless, a satisfactory fit for all other elements combined with the rigidity of polyoxotungstate part allows for a reliable determination of the materials' compositions.

XRD measurements details: Single-crystal diffraction data were collected at 100 K on a STOE STADIVARI diffractometer for **KN-1** and on a SuperNova (Rigaku) diffractometer for **KN-2** with MoKα radiation ($\lambda = 0.71073$ Å). The crystals were mounted in a Hampton cryoloop with Paratone-N oil to prevent water loss. Absorption corrections were done by Gaussian integration over a multifaceted crystal model using either STOE X-Red32 software[19] with the following scaling of reflection intensities was performed within STOE LANA[20] for **KN-1** and with a CrysAlis software for **KN-2**.[21]

The structures were solved by direct methods and refined by full-matrix least-squares method against $|F|^2$ with anisotropic thermal parameters for all heavy atoms (W, P, Mn, Cu, K and Na) employing the SHELXTL software package.[22] ISOR restrictions had to be applied to get reasonable anisotropic displacement parameters for some disordered K and Na. Hydrogen atoms of water molecules were not located.

The refinement of the relative site occupancy factors (s.o.f.) for W14 and Mn^{II} centers in **KN-1** as well as W27/Cu1 and W28/Cu2 positions in **KN-2** with a combination of PART/EADP or EXYZ/PART/EADP commands, respectively, yielded 50%/50% occupancies in all the cases. Therefore, after such refinement the s.o.f. for the corresponding positions were fixed at 0.5 and refined normally. The sodium cation in the central cavity of polyanions $\{Mn^{II}P_4W_{27}\}$ in **KN-1** was disordered with an O atom of the water molecule coordinated to the Mn^{II} ion. The s.o.f. for these atoms were first refined using a combination of EXYZ/PART/EADP instructions and then fixed at the obtained values (~0.5). The relative s.o.f. for the disordered positions of O atoms of solvent and coordinated water molecules as well as potassium and sodium counter ions were first refined in an isotropic approximation with $U_{iso} = 0.05$ and then fixed at the obtained values and refined without the thermal parameter restrictions. Some of the disordered K (K4/K4A, K5/K5A and K6/K6A) and O (O6W/O6H) positions in **KN-2** structure were refined with a combination of PART/EADP commands.

Due to severe disorder we were not able to locate all the crystal water molecules as well as a part of Na^+ and K^+ counter cations in these structures. Therefore, after we have assigned all electron density peaks, we could, a SQUEEZE procedure was applied to treat diffused electron density in the voids. The final formulae used herein and in the CIFs were determined by a combination of single

Table 3. Crystallographic data and structure refinement for **KN-1** and **KN-2**.

Sample	KN-1	KN-2
Empirical formula	$H_{56}K_{10}MnNa_4O_{127}P_4W_{27}$	$H_{61.5}CuK_{11}Na_{2.5}O_{129}P_4W_{27}$
Formula weight/g mol^{-1}	7714.17	7764.85
Crystal system	Monoclinic	Monoclinic
Space group	*C*2/*c*	*C*2/*c*
a/Å	30.860(6)	30.1112(3)
b/Å	18.004(4)	19.6135(2)
c/Å	23.913(5)	43.7229(4)
β	114.97(3)°	94.165(1)°
Volume/Å^3	12044(5)	25753.9(4)
Z	4	8
D_{calc}/g cm^{-3}	4.254	4.005
Absorption coefficient/mm^{-1}	26.302	24.698
F(000)	13556	27328
Crystal size/mm^3	0.06×0.07×0.11	0.24×0.30×0.34
2Θ range for data collection	2.26°–25.02°	3.16°–25.03°
Completeness to Θ_{max}	99.7%	99.8%
Index ranges	$-36<h<31$, $-19<k<21$, $-28<l<28$	$-35<h<35$, $-23<k<22$, $-50<l<52$
Reflections collected	85326	128549
Independent reflections	10622	22711
R_{int}	0.1026	0.0859
Observed ($I>2\sigma(I)$)	8257	18233
Absorption correction	Numerical (Gaussian integration)	
T_{min}/T_{max}	0.0012/0.0073	0.0340/0.3340
Data/restraints/parameters	10622/90/548	22711/42/1034
Goodness-of-fit on F^2	1.032	1.095
R_1, wR_2 ($I>2\sigma(I)$)	$R_1=0.0631$, $wR_2=0.1713$	$R_1=0.0535$, $wR_2=0.1276$
R_1, wR_2 (all data)	*$R_1=0.0786$, $wR_2=0.1795$*	$R_1=0.0715$, $wR_2=0.1390$
Largest diff. peak and hole/e Å^{-3}	4.200/−3.160	5.018/−2.673

crystal X-ray (polyanion part), elemental and thermogravimetric (exact number of cations and solvent molecules) analyses.

Additional crystallographic data are summarized in Table 3. Deposition numbers 2033137 (**KN-1**) and 2033138 (**KN-2**)) contain(s) the supplementary crystallographic data for this paper. These data are provided free of charge by the joint Cambridge Crystallographic Data Centre and Fachinformationszentrum Karlsruhe Access Structures service.

Acknowledgements

We gratefully acknowledge financial support by Forschungszentrum Jülich and EU ERC Starting Grant 308051 – MOLSPINTRON. T. I. appreciates The Punjab Educational Endowment Fund (PEEF) for a doctoral fellowship (CMMS scholarship program). Open access funding enabled and organized by Projekt DEAL.

Conflict of Interest

The authors declare no conflict of interest.

Keywords: Polyoxometalates · single-crystal X-ray analysis · electrochemistry · magnetochemistry

[1] *See for example*: a) O. Oms, A. Dolbecq, P. Mialane, *Chem. Soc. Rev.* **2012**, *41*, 7497–7536; b) S.-T. Zheng, G.-Y. Yang, *Chem. Soc. Rev.* **2012**, *41*, 7623–7646; c) J.-W. Zhao, Y.-Z. Li, L.-J. Chen, G.-Y. Yang, *Chem. Commun.* **2016**, *52*, 4418–4445.

[2] *See for example*: a) O. A. Kholdeeva, N. V. Maksimchuk, G. M. Maksimov, *Catal. Today* **2010**, *157*, 107–113; b) N. Mizuno, K. Kamata, *Coord. Chem. Rev.* **2011**, *255*, 2358–2370; c) A. Patel, N. Narkhede, S. Singh, S. Pathan, *Catal. Rev.* **2016**, *58*, 337–370; d) Q. Han, Y. Ding, *Dalton Trans.* **2018**, *47*, 8180–8188; e) M. B. Ahicart, J. S. López, J. J. Carbó, J. M. Poblet, J. R. G. Mascaros, *Nat. Chem.* **2018**, *10*, 24–30; f) D. Gao, I. Trentin, L. Schwiedrzik, L. González, C. Streb, *Molecules* **2019**, *25*, 157, 1–22.

[3] *See for example*: a) A. Müller, F. Peters, *Chem. Rev.* **1998**, *98*, 239–271; b) J. M. Clemente-Juan, E. Coronado, A. Gaita-Arino, *Chem. Soc. Rev.* **2012**, *41*, 7434–7478; c) X.-J. Feng, Y.-G. Li, Z.-M. Zhang, E. Wang, *Acta Chim. Sin.* **2013**, *71*, 1575–1588; d) N. V. Izarova, P. Kögerler, *Trends in Polyoxometalates Research* (Eds.: L. Ruhlmann, D. Schaming), Nova Science Publishers: Hauppauge, **2015**, pp. 121–149.

[4] B. Dawson, *Acta Crystallogr.* **1953**, *6*, 113–126.

[5] M. T. Pope, *Heteropoly and Isopoly Oxometalates*, Springer, Berlin, **1983**.

[6] *See for example*: a) A. Proust, R. Thouvenot, P. Gouzerh, *Chem. Commun.* **2008**, *16*, 1837–1852; b) A. Proust, B. Matt, R. Villanneau, G. Guillemot, P. Gouzerh, G. Izzet, *Chem. Soc. Rev.* **2012**, *41*, 7605–7622; c) X. Ma, H. Li, L. Chen, J. Zhao, *Dalton Trans.* **2016**, *45*, 4935–4960; d) Z.-J. Liu, X.-L. Wang, C. Qin, Z.-M. Zhang, Y.-G. Li, W.-L. Chen, E.-B. Wang, *Coord. Chem. Rev.* **2016**, *313*, 94–110; e) V. Das, R. Kaushik, F. Hussain, *Coord. Chem. Rev.* **2020**, *413*, 213271–213292.

[7] a) R. Contant, *Inorganic Synthesis, Vol. 27*, Ed: A. P. Ginsberg, John Wiley and Sons: New York, 1 **990**; pp. 104–111; b) R. Contant, J. P. Ciabrini, *J. Chem. Res. Synop.* **1977**, 222; *J. Chem. Res. Miniprint* **1977**, 2601; c) R. Contant, A. Tézé, *Inorg. Chem.* **1985**, *24*, 4610–4614.

[8] a) B. Godin, Y.-G. Chen, J. Vaissermann, L. Ruhlmann, M. Verdaguer, P. Gouzerh, *Angew. Chem.* **2005**, *117*, 3132–3135; *Angew. Chem. Int. Ed. Engl.* **2005**, *44*, 3072–3075; Pages; b) E. Ruiz, J. Cano, S. Alvarez, P. Gouzerh, M. Verdaguer, *Polyhedron* **2007**, *26*, 2161–2164; c) D. Zhang, C. Zhang, P. Ma, B. S. Bassil, R. Al-Oweini, U. Kortz, J. Wang, J. Niu, *Inorg. Chem. Front.* **2015**, *2*, 254–262; d) D. Zhang, F. Cao, P. Ma, C. Zhang, Y. Song, Z. Liang, X. Hu, J. Wang, J. Niu, *Chem. Eur. J.* **2015**, *21*, 17683–17690.

[9] a) S. S. Mal, U. Kortz, *Angew. Chem.* **2005**, *117*, 3843–3846; *Angew. Chem. Int. Ed.* **2005**, *44*, 3777–3780; b) S. S. Mal, B. S. Bassil, M. Ibrahim, S. Nellutla, J. van Tol, N. S. Dalal, J. A. Fernández, X. López, J. M. Poblet, R. Ngo Biboum, B. Keita, U. Kortz, *Inorg. Chem.* **2009**, *48*, 11636–11645; c) C. Pichon, P. Mialane, A. Dolbecq, J. Marrot, E. Rivière, B. Keita, L. Nadjo, F. Sécheresse, *Inorg. Chem.* **2007**, *46*, 5292–5301; d) S. S. Mal,

M. H. Dickman, U. Kortz, A. M. Todea, A. Merca, H. Bögge, T. Glaser, A. Müller, S. Nellutla, N. Kaur, J. van Tol, N. S. Dalal, B. Keita, L. Nadjo, *Chem. Eur. J.* **2008**, *14*, 1186–1195; e) M. Ibrahim, I. M. Mbomekallé, P. de Oliveira, G. E. Kostakis, C. E. Anson, *Dalton Trans.* **2019**, *48*, 15545–15552; f) A. Müller, M. T. Pope, A. M. Todea, H. Bögge, J. van Slageren, M. Dressel, P. Gouzerh, R. Thouvenot, B. Tsukerblat, A. Bell, *Angew. Chem.* **2007**, *119*, 4561–4564; *Angew. Chem. Int. Ed.* **2007**, *46*, 4477–4480; g) F. L. Sousa, H. Bögge, A. Merca, P. Gouzerh, R. Thouvenot, A. Müller, *Chem. Commun.* **2009**, 7491–7493; h) V. S. Korenev, S. Floquet, J. Marrot, M. Haouas, I. M. Mbomekallé, F. Taulelle, M. N. Sokolov, V. P. Fedin, E. Cadot, *Inorg. Chem.* **2012**, *51*, 2349–2358; i) P. Yang, M. Alsufyani, A.-H. Emwas, C. Chen, N. M. Khashab, *Angew. Chem.* **2018**, *130*, 13230–13235; *Angew. Chem. Int. Ed.* **2018**, *57*, 13046–13051.

[10] a) F. Hussain, U. Kortz, B. Keita, L. Nadjo, M. T. Pope, *Inorg. Chem.* **2006**, *45*, 761–766; b) Z. Zhang, S. Yao, Y. Qi, Y. Li, Y. Wang, E. Wang, *Dalton Trans.* **2008**, 3051–3053.

[11] X. Yi, N. V. Izarova, P. Kögerler, *Chem. Commun.* **2018**, *54*, 2216–2219.

[12] a) I. D. Brown, D. Altermatt, *Acta Crystallogr.* **1985**, *B41*, 244–247; b) K. Knížek, Kalvados – *Software for crystal structure and powder diffraction*; see http://www.fzu.cz/~knizek/kalvados/index.html.

[13] The hydrated Na/K salt of $\{[Co(H_2O)_4]_2[\{(H_2O)_4Co\}(C_6H_5PO)_2P_4W_{24}O_{92}]\}_n^{10n-}$. *Synthesis*: A solution of $CoCl_2\cdot 6H_2O$ (0.0334 g, 0.141 mmol) in 0.5 M NaOAc (pH 4.8; 5 mL) was added to a solution of **KLD-{$P_4W_{24}(PhP)_2$}** (0.1 g, 0.14 mmol) in 0.5 M NaOAc (pH 4.8; 10 mL) under a vigorous string at 70 °C. The resulting reaction mixture with pH 4.6 was then placed in an oven and kept at 70 °C for 3 days. The obtained pink colored reaction solution was then cooled to room temperature followed by addition of 1 M dimethylammonium chloride solution in water (2 mL). The resulting solution was divided into four equal portions and left for evaporation in open vials. Pink block-shaped crystals of the product appeared after 2 weeks. *Unit cell*: Monoclinic, $C2$, = 18.746(2) Å, b = 28.6236(5) Å, c = 14.1747(8) Å, β = 116.177(11)°, V = 6825.98(8) Å^3, Z = 2.

[14] a) X.-Y. Zhang, M. T. Pope, M. R. Chance, G. B. Jameson, *Polyhedron* **1995**, *14*, 1381–1392; b) J. J. Cowan, A. J. Bailey, R. A. Heintz, B. T. Do, K. I. Hardcastle, C. L. Hill, I. A. Weinstock, *Inorg. Chem.* **2001**, *40*, 6666–6675; c) B. S. Bassil, M. H. Dickman, M. Reicke, U. Kortz, B. Keita, L. Nadjo, *Dalton Trans.* **2006**, 4253–4259; d) B. S. Bassil, M. Ibrahim, R. Al-Oweini, M. Asano, Z. Wang, J. van Tol, N. S. Dalal, K.-Y. Choi, R. Ngo Biboum, B. Keita, L. Nadjo, U. Kortz, *Angew. Chem.* **2011**, *123*, 6083–6087; *Angew. Chem. Int. Ed.* **2011**, *50*, 5961–5964; e) R. Al-Oweini, A. Sartorel, B. S. Bassil, M. Natali, S. Berardi, F. Scandola, U. Kortz, M. Bonchio, *Angew. Chem.* **2014**, *126*, 11364–11367; *Angew. Chem. Int. Ed.* **2014**, *53*, 11182–11185; f) R. Al-Oweini, B. S. Bassil, J. Friedl, V. Kottisch, M. Ibrahim, M. Asano, B. Keita, G. Novitchi, Y. Lan, A. Powell, U. Stimming, U. Kortz, *Inorg. Chem.* **2014**, *53*, 5663–5673; g) R. Gupta, I. Khan, F. Hussain, A. M. Bossoh, I. M. Mbomekallé, P. de Oliveira, M. Sadakane, C. Kato, K. Ichihashi, K. Inoue, S. Nishihara, *Inorg. Chem.* **2017**, *56*, 8759–8767.

[15] a) B. Keita, I. M. Mbomekalle, L. Nadjo, *Electrochem. Commun.* **2003**, *5*, 830–837; b) D. Jabbour, B. Keita, L. Nadjo, U. Kortz, S. S. Mal, *Electrochem. Commun.* **2005**, *7*, 841–847; c) Z.-J. Liu, Z.-M. Zhang, H. Fu, Y.-G. Li, W.-L. Chen, H. H. Wu, E.-B. Wang, *Dalton Trans.* **2012**, *41*, 11700–11705; d) B. S. Bassil, A. Haider, M. Ibrahim, A. S. Mougharbel, S. Bhattacharya, J. H. Christian, J. K. Bindra, N. S. Dalal, M. Wang, G. Zhang, B. Keita, I. A. Rutkowska, P. J. Kulesza, U. Kortz, *Dalton Trans.* **2018**, *47*, 12439–12448; e) X. Yi, N. V. Izarova, T. Iftikhar, J. van Leusen, P. Kögerler, *Inorg. Chem.* **2019**, *58*, 9378–9386.

[16] a) J. P. Launay, *J. Inorg. Nucl. Chem.* **1976**, *38*, 807–816; b) B. Keita, Y. W. Lu, L. Nadjo, R. Contant, *Electrochem. Commun.* **2000**, *2*, 720–726; c) J.-J. Chen, M. D. Symes, L. Cronin, *Nat. Chem.* **2018**, *10*, 1042–1047.

[17] a) H. Lueken, *Magnetochemie*, Teubner Verlag, Stuttgart, **1999**; b) J. S. Griffith, *The Theory of Transition-Metal Ions*, Cambridge University Press, Cambridge, **1980**.

[18] M. Speldrich, J. van Leusen, P. Kögerler, *J. Comput. Chem.* **2018**, *39*, 2133–2145.

[19] STOE X-Red32, absorption correction by Gaussian integration, analogous to P. Coppens, The Evaluation of Absorption and Extinction in Single-Crystal Structure Analysis. Crystallographic Computing (Ed.: F. R. Ahmed), Munksgaard, Copenhagen, **1970**, pp. 255–270.

[20] J. Koziskova, F. Hahn, J. Richter, J. Kozisek, *Acta Chim. Slov.* **2016**, *9*, 136–140.

[21] CrysAlisPro, Version 1.171.39.46 (Rigaku Oxford Diffraction, **2018**).

[22] G. M. Sheldrick, *Acta Crystallogr.* **2015**, *C71*, 3–8.

Manuscript received: November 10, 2020
Accepted manuscript online: April 7, 2021
Version of record online: May 13, 2021

